


Structural basis for ligand capture and release by the endocytic receptor ApoER2

Hidenori Hirai^{1,†}, Norihisa Yasui^{2,†}, Keitaro Yamashita³, Sanae Tabata¹, Masaki Yamamoto³, Junichi Takagi¹ & Terukazu Nogi^{4,*} 

Abstract

Apolipoprotein E receptor 2 (ApoER2) is a close homologue of low-density lipoprotein receptor (LDLR) that mediates the endocytosis of ligands, including LDL particles. LDLR family members have been presumed to explore a large conformational space to capture ligands in the extended conformation at the cell surface. Ligands are subsequently released through a pH-titrated structural transition to a self-docked, contracted-closed conformation. In addition to lipoprotein uptake, ApoER2 is implicated in signal transduction during brain development through capture of the extracellular protein reelin. From crystallographic analysis, we determine that the full-length ApoER2 ectodomain adopts an intermediate contracted-open conformation when complexed with the signaling-competent reelin fragment, and we identify a previously unappreciated auxiliary low-affinity binding interface. Based on mutational analyses, we propose that the pH shift during endocytosis weakens the affinity of the auxiliary interface and destabilizes the ligand–receptor complex. Furthermore, this study elucidates that the contracted-open conformation of ligand-bound ApoER2 at neutral pH resembles the contracted-closed conformation of ligand-unbound LDLR at acidic pH in a manner suggestive of being primed for ligand release even prior to internalization.

Keywords ApoER2; endocytic receptor; LDLR family; ligand uptake; reelin

Subject Categories Membrane & Intracellular Transport; Signal Transduction; Structural Biology

DOI 10.15252/embr.201643521 | Received 14 October 2016 | Revised 9 March 2017 | Accepted 15 March 2017 | Published online 26 April 2017

EMBO Reports (2017) 18: 982–999

Introduction

Low-density lipoprotein receptor (LDLR) binds LDL particles at the cell surface, and the complex internalizes through endocytosis [1]. After internalization, the LDL particles dissociate from LDLR in the early endosome and are delivered to the lysosome where they are

degraded. Meanwhile, LDLR is recycled back to the cell surface for further uptake of LDL. Since LDLR plays a pivotal role in the clearance of LDL from blood plasma, deletion or defects of LDLR increase LDL levels, causing familial hypercholesterolemia (FH) [2,3]. LDLR is a type I membrane protein, and its ectodomain contains an N-terminal tandem repeat of seven LDLR type-A (LA1–7) modules followed by an epidermal growth factor precursor homology (EGFPH) domain [4,5]. The EGFPH domain consists of two EGF-like modules (EGF-A and EGF-B), a YWTD β -propeller [6,7], and an additional EGF-like module (EGF-C). Each \sim 40 amino acid residue LA module generally assumes a compact disulfide-knotted structure containing a Ca^{2+} -coordinated acidic residue cluster and an aromatic residue, constituting a putative ligand-binding site [8–14]. Although the LA modules always occur as a set of multiple repeats in LDLR and its homologues, ligand recognition is often mediated by particular subset of the module repeat segment [15]. Several crystal structures of the LA module from LDLR family members have been determined in complex with non-LDL ligands, such as receptor-associated protein (RAP) and virus coat protein [16,17], conforming to a canonical ligand recognition mode: LA modules commonly accommodate a Lys side chain of the ligand into a pocket surrounded by the conserved acidic cluster and the aromatic residue. LA modules presumably recognize LDL and other lipoproteins through a similar mechanism given that the major components of lipoproteins, apoB and apoE, have an abundance of basic residues [16,18].

Dissection of this potential mechanism requires a structure-based understanding of the interaction between LDLR and its ligands at the cell surface. A moderate-resolution structure of the full-length LDLR ectodomain has been previously determined by X-ray crystallography [19]. The structure showed a hairpin-like self-docked conformation, in which linearly arranged LA1–7 modules are contracted by EGF modules and cover the top face of the YWTD β -propeller domain. Since the ectodomain was crystallized under slightly acidic conditions at pH 5.3, this conformation was thought to reflect the binding-inactive state of the receptor (hereafter defined as a contracted-closed conformation) in the endosomal compartment. The structure of the same LDLR ectodomain has also been determined in complex with protein

¹ Institute for Protein Research, Osaka University, Osaka, Japan

² Graduate School of Medicine, Dentistry and Pharmaceutical Sciences, Okayama University, Okayama, Japan

³ RIKEN SPring-8 Center, Hyogo, Japan

⁴ Graduate School of Medical Life Science, Yokohama City University, Yokohama, Japan

*Corresponding author. Tel: +81 45 508 7226; Fax: +81 45 508 7365; E-mail: nogi@tsurumi.yokohama-cu.ac.jp

[†]These authors contributed equally to this work

convertase subtilisin/kexin type 9 (PCSK9) under neutral conditions of pH 7.0 [20]. PCSK9 is known to serve as a regulatory protein of LDLR to promote its degradation [21,22]. In contrast to the contracted-closed LDLR structure under acidic conditions, the LDLR ectodomain bound by PCSK9 exhibited an extended conformation. Because the LA modules are liberated from the YWTD domain due to a swing motion of EGF modules at neutral pH in this extended, or extended-open, conformation, it has been presumed that the ectodomain becomes more flexible to explore a large conformational space and capture its binding partners. The structural analysis raised the possibility that PCSK9, unlike other LDLR ligands, binds with the EGF-A module of LDLR to prevent EGF modules from arranging as observed in the contracted-closed conformation [20]. The detailed molecular mechanism of the ligand release, however, still remains elusive, as no physiological ligand-complex structures are available for the entire ectodomain of LDLR or for its closely related homologues. Unfortunately, crystallization of the LDLR:LDL complex for structural analysis is expected to be extremely difficult due to the fact that the chemical composition of the LDL particle is inhomogeneous. Structural analysis of LDL bound to LDLR by cryo-electron microscopy has suggested that the YWTD domain interacts with LDL, but the conformation of the entire ectodomain remains unresolved [23].

Invoked by the dilemma described above, we hypothesized that an informative model of LDLR function could be developed by determining a functionally relevant structure of an LDLR family member in a ligand-bound complex that is more amenable to crystallographic analyses. Among the variety of LDLR family members, apolipoprotein E receptor 2 (ApoER2) shows significant similarities to LDLR in both domain organization and function [24,25]. The ectodomain of ApoER2 consists of the same set of structural modules in the same order as LDLR although splicing variants containing different numbers of the LA repeats in the ligand-binding domain are identified for ApoER2 [26,27]. Moreover, ApoER2 mediates the uptake of apoE-containing lipoproteins via endocytosis [27]. In addition to lipoprotein uptake, ApoER2 binds the extracellular protein reelin to mediate the signal transduction that regulates cortical layer formation during brain development [28]. Reelin is a gigantic glycoprotein that contains a characteristic concatenation of eight repeats termed “reelin repeats” [29]. It has been established that the fifth and sixth reelin repeats (R56) comprise the signaling-competent fragment and interact with ApoER2 primarily using the first LA module (LA1) [30]. X-ray crystallographic analysis demonstrated that LA1 of ApoER2 captures a Lys residue on reelin with a conserved acidic–aromatic pocket [31], indicating that reelin is recognized by ApoER2 via the canonical ligand-binding mechanism of the LDLR family. Hence, we chose the ApoER2–reelin pair as a model

to explore the structural mechanism of ligand recognition by the LDLR family members.

In this study, we determined the crystal structure of the ApoER2 ectodomain in complex with the reelin R56 fragment and found that the receptor assumes a contracted-open conformation by engaging the ligand through multiple binding interfaces. The resulting structure, combined with surface plasmon resonance analysis under neutral and acidic pH, provides important clues for understanding the mechanism by which LDLR family members release ligands in the endosomal compartment.

Results

Quantitative binding analysis between ApoER2 ectodomain and reelin R56

To quantify the affinity of the ApoER2 and reelin R56 binding interaction, we first performed surface plasmon resonance (SPR) analysis using the entire ectodomain fragment of the human ApoER2 splicing variant lacking LA4-6. It is known that this ApoER2 variant is expressed in human brain tissue [32] and that the same variant serves as the receptor for reelin in mouse [33,34]. The ApoER2 ectodomain (ApoER2 ECD) fragment was immobilized on the sensor chip, and the reelin R56 fragment was injected over the sensor chip surface. The dissociation constant between ApoER2 ECD and reelin R56 was estimated to be 1.2×10^{-8} M at pH 7.5 by steady-state analysis (Fig 1A, Table 1). In addition, SPR measurements performed at pH 5.5 resulted in a drastic increase in the dissociation constant (Fig 1B, Table 1). Our results indicate that the binding affinity of the reelin R56 fragment for ApoER2 decreases after endocytosis, similarly to that of the LDL particle for LDLR. In our previous work, we performed an analogous experiment using only the LA1 module of ApoER2. There we found the dissociation constant between LA1 and reelin R56 at neutral pH to be 7.3×10^{-8} M, a fivefold in comparison with the full-length ApoER2 ECD in this work. It was also observed that R56 dissociates from the full-length ApoER2 ECD relatively slowly compared with the partial fragments, as was consistent with our preliminary analysis [30]. As shown in Fig 1A, the response curve of the ApoER2 ECD–R56 interaction in the present analysis drops gradually after the end of injection. In contrast, it has been observed in our previous work that the curve drops almost directly to baseline in case of the partial fragments including the LA1 fragment [31]. We therefore expected that the ApoER2 ECD possesses auxiliary low-affinity binding interfaces except for LA1, which would contribute to the stabilization of the ligand complex.

Figure 1. Steady-state analysis of SPR data #1: Estimation of dissociation constants and exploration of binding interfaces.

A, B Estimation of dissociation constants at (A) pH 7.5 and (B) pH 5.5. A representative result from triplicate SPR measurements is plotted for each condition. To obtain overlaid sensorgrams, serially diluted reelin R56 fragments were injected over a sensor chip surface with ApoER2 ECD fragments immobilized through biotin–streptavidin interactions (inset). Equilibrium response (R_{eq}) values were plotted against the concentration of injected R56 to calculate the dissociation constants (K_D). The K_D value for each condition is listed as the mean of triplicates with the standard deviation in Table 1.

C–F Introduction of salt bridge-disrupting mutations to LA modules: (C) D68N in LA1, (D) E107Q in LA2, (E) E150Q in LA3, and (F) E191Q in LA7.

Source data are available online for this figure.

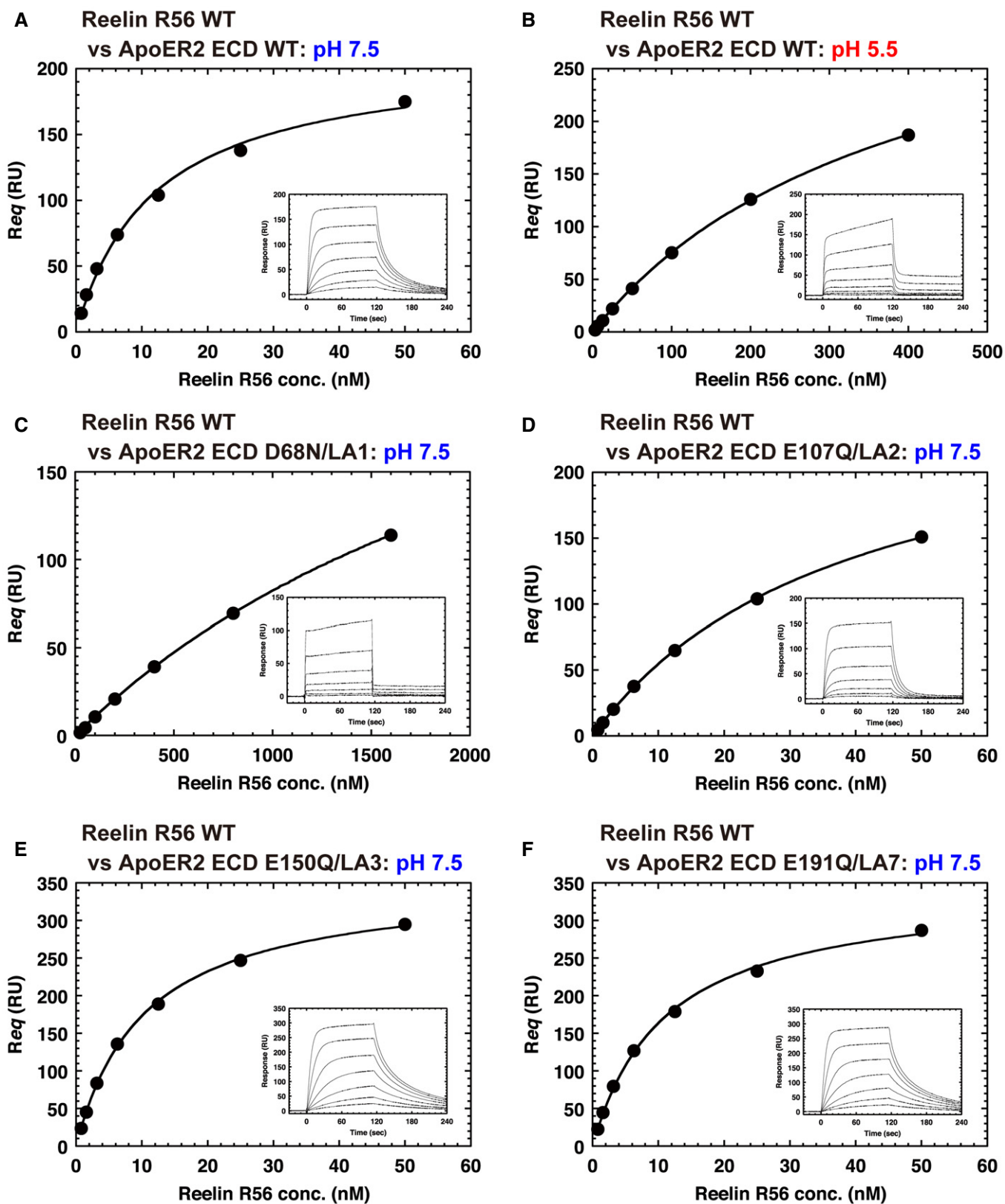


Figure 1.

Table 1. Summary of SPR analysis #1: Estimation of dissociation constants and exploration of binding interfaces.

Analyte (reelin R56)	Ligand (ApoER2 ECD)	pH	Ca ²⁺ conc.	K _D (M) ^a	P-value
Wild type	Wild type	7.5	2 mM	$(1.2 \pm 0.1) \times 10^{-8}$	
		5.5	2 mM	$(4.1 \pm 0.3) \times 10^{-7}$	
Wild type	D68N/LA1	7.5	2 mM	$(2.8 \pm 0.1) \times 10^{-6}$ ^b	0.00061 ^c
Wild type	E107Q/LA2	7.5	2 mM	$(3.8 \pm 0.2) \times 10^{-8}$	0.00002 ^c
Wild type	E150Q/LA3	7.5	2 mM	$(1.0 \pm 0.0) \times 10^{-8}$	
Wild type	E191Q/LA4	7.5	2 mM	$(1.1 \pm 0.0) \times 10^{-8}$	

^aEach K_D value represents the mean of triplicate SPR measurements with standard deviation. Processing of the sensorgram and curve fitting of affinity analysis were performed separately in the triplicate experiments, and the three obtained K_D values were used to calculate the mean, standard deviation, and P-value.

^bThe actual K_D value should be higher than the reported value since the highest concentration of the analyte in the SPR measurement was lower than the estimated K_D value.

^cThe difference of the K_D value compared with that calculated for the interaction between reelin R56 wild type versus ApoER2 ECD wild type at pH 7.5 is statistically significant with the indicated P-value, which is calculated by the unpaired two-tailed t-test.

Identification of a low-affinity binding interface within the ApoER2 LA modules

To explore the binding sites in regions other than the LA1 module, we next designed a series of ApoER2 ECD derivatives to perturb the affinity of candidate interfaces. For each mutation, a specific acidic residue was mutated to disrupt potential salt bridges in the putative ligand-binding interface of the respective LA module (LA1: D68N, LA2: E107Q, LA3: E150Q, and LA7: E191Q, respectively; Fig EV1). The mutated acidic residues are not involved in the coordination of calcium ions unlike other acidic residues in the cluster. Therefore, the introduced mutations are thought to partially weaken the binding affinity for basic residues, while maintaining the structural integrity of the respective LA modules. Consistent with previous binding and structural analyses, the mutation in LA1 drastically reduced the binding affinity for R56 ($K_D > 2.8 \times 10^{-6}$ M; Fig 1C, Table 1). In addition, the LA2 mutant also showed a three-fold reduction in affinity ($K_D = 3.8 \times 10^{-8}$ M; Fig 1D, Table 1), whereas the affinities of the LA3 and LA7 mutants were in the same range as that of the wild type (Fig 1E and F, Table 1). These results strongly indicate that the LA2 module is involved in the complex formation.

Structure determination of the entire ApoER2 ectodomain in complex with reelin R56

To elucidate the details of the complex formation, we then determined the X-ray crystal structure of the entire ApoER2 ECD in complex with the reelin R56 fragment (Fig 2). Co-crystals were obtained under neutral conditions of pH 7.5 using constructs of the two proteins expressed in mammalian cells. The R56 fragment was selenomethylated for single-wavelength anomalous diffraction (SAD) phasing. The initial model for the complex was built against an electron density map at 3.2 Å resolution. The crystal contains two nearly identical complexes in the asymmetric unit. The electron density for R56 is relatively clear, producing a model consistent with a crystal structure determined for unbound reelin R56 [30]. R5 and R6 are composed of two homologous subrepeats (subrepeats A and B) and an intervening EGF-like module, respectively, and are arranged side by side. Interestingly, the overall structure of ApoER2 ECD seems similar to the contracted-closed

conformation of LDLR crystallized under the acidic conditions [19]. The interface between R56 and LA1 (referred to as Interface-1) is also almost identical to that observed in the crystallographic analysis of the R56:LA1 complex (Fig 3A) [31]. In the present structure, the N-terminal LA modules are folded back toward the YWTD propeller domain, but they form no direct contacts between them.

The model of ApoER2 contains some ambiguity in the region between LA2 and EGF-A due to disorder (Fig 2A and B). We could not observe significant electron densities for LA3 and LA7, whereas density for EGF-A was weak but still clear enough to build a reliable model using the NMR structure of LDLR EGF-AB unit as a reference (PDB code: 1HJ7) [35]. Although we expect the LA2 module to interact with R56 based on the SPR analysis, LA2 appears to be highly mobile. The electron density corresponding to LA2 was undoubtedly present in the region following the C-terminus of LA1, but it was impossible to confidently trace the backbone of LA2 in the electron density map.

Assignment of the LA2 model by constrained real space fragment search

To assign a reliable model of LA2 against the weak electron density, we separately determined a high-resolution structure of a partial fragment containing LA2 and fitted it into the electron density of the complex crystal as a rigid body. For this purpose, the LA12 fragment was produced in *E. coli* and crystallized after refolding in redox buffer. The resulting LA12 structure determined at 1.9 Å resolution showed an extended arrangement where the respective ligand-binding surfaces of the two LA modules were pointed in opposite directions (Fig 2C). In fact, the LA2 model did not overlap with the observed weak electron densities when we aligned the LA12 structure onto the LA1 module in the complex. The relative orientation of LA1 and LA2 seems to be restricted by the hydrogen-bonding network in the inter-module linker and by the intimate interactions with symmetry neighbors in the crystal. In general, the inter-LA arrangement is presumed to be flexible among the LDLR family members. In LDLR, for instance, the LA3-LA4 arrangement in the contracted-closed ectodomain structure under the acidic conditions [19] is significantly different from that in the LA34 fragment in complex with RAP [16]. We therefore postulated that LA12 in the

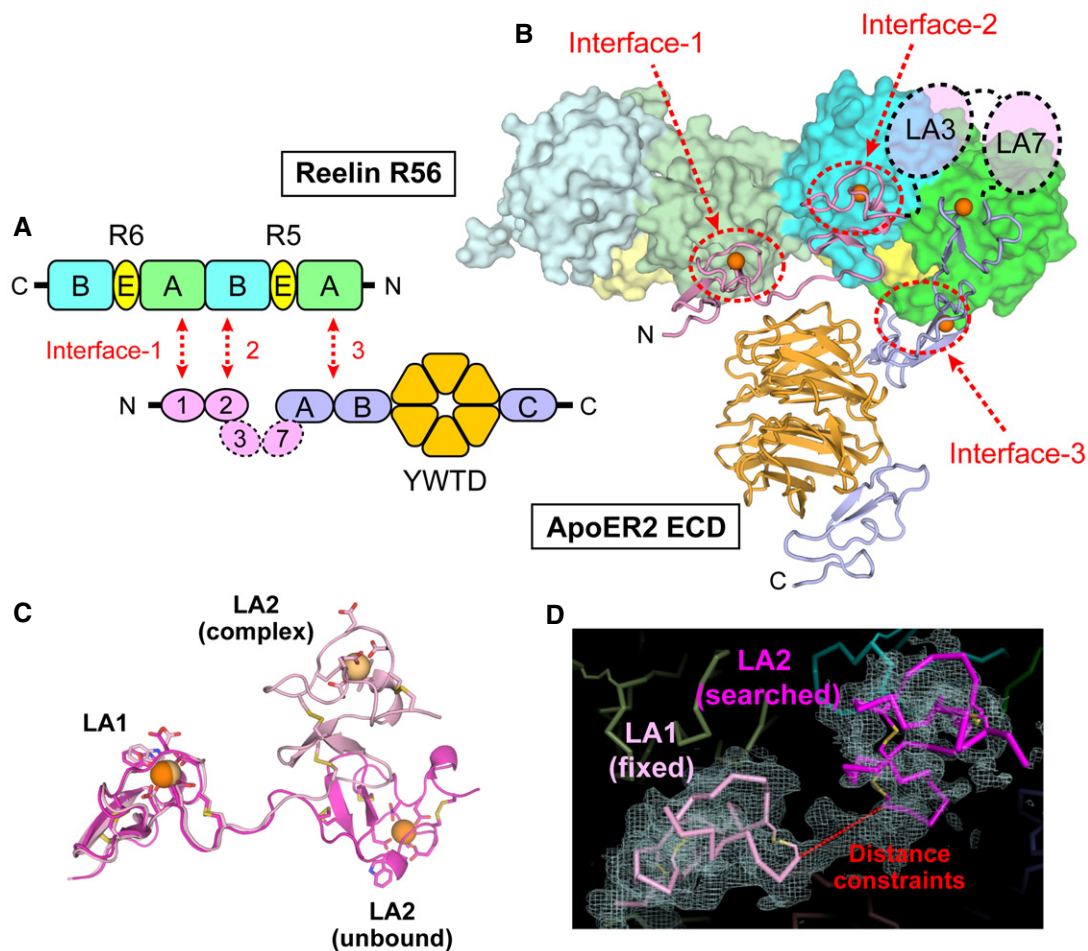


Figure 2. Structure of the ApoER2 ECD:reelin R56 complex.

- A** Domain organization of the reelin R56 and ApoER2 ECD fragments used for structure determination. Both of the two reelin repeats, R5 and R6, are composed of a subrepeat A (green), an EGF-like module (yellow), and a subrepeat B (cyan). ApoER2 contains four LA modules, LA1, 2, 3, and 7 (magenta), three EGF-like modules, EGF-A, EGF-B, and EGF-C (blue), and a YWTD repeat (orange). The complex is maintained through three binding interfaces (red dotted arrows). The modules with disordered electron density (LA3 and 7) are indicated with a dotted line.
- B** Crystal structure of the complex. The reelin R56 and ApoER2 ECD fragments are displayed as surface and ribbon models, respectively. Four calcium ions (orange spheres) were included in the final model of ApoER2 ECD. It is probable that the LA3 and 7 modules connect the C-terminus of LA2 and the N-terminus of EGF-A in a hairpin-like configuration, although they are not assigned in the final model, as indicated with dotted circles in magenta.
- C** Inter-module arrangement of the LA12 fragment. The crystal structures of the unbound LA12 fragment (dark) and in complex with reelin R56 (light) are superposed on LA1. The residues constituting the respective binding interfaces of the two modules are depicted as stick models, and the calcium ions are shown as orange spheres.
- D** Procedure of real space fragment search. The coordinates of LA2 (dark magenta) were extracted from the crystal structure of unbound LA12 and manually located at the center of the electron density blob of the $2mF_o - DF_c$ map (mesh). The LA1 model (light magenta) was fixed at the position assigned based on the electron density. The orientation and position of LA2 was searched and scored by electron density values with inter-module distance constraints (red dotted line). After the LA2 model with the highest score was chosen, the model of the inter-module linker was manually built and refined.

ApoER2 complex also rearranges by a hinge motion at the inter-module linker, thereby suitably placing LA2 for interaction with R56. We fitted the LA2 model by a constrained real space fragment search (Fig 2D). This procedure searched the position and orientation of the LA2 model, which maximized electron density values at atomic positions, while constraining the distance between LA1 and LA2. As a result, similar solutions were obtained for both of the two complexes in the asymmetric unit of the crystal, where LA2 is located close to the bottom face of reelin R5B. (Hereafter, the interface between LA2 and reelin R5B is referred to as Interface-2.)

This interaction mode is consistent with the canonical ligand-binding mode as observed in other LA–ligand pairs including Interface-1 of the ApoER2 ECD:reelin R56 complex. Importantly, the acidic residue cluster on the ligand-binding surface of LA2 is oriented to the side chain of K2194 on reelin R5B despite the lack of imposed distance restraints between them during the constrained real space search. Although several other solutions showed high scores in the search, most of them placed the LA2 model in similar positions and orientations to those in the top solution (Fig EV2A and B).

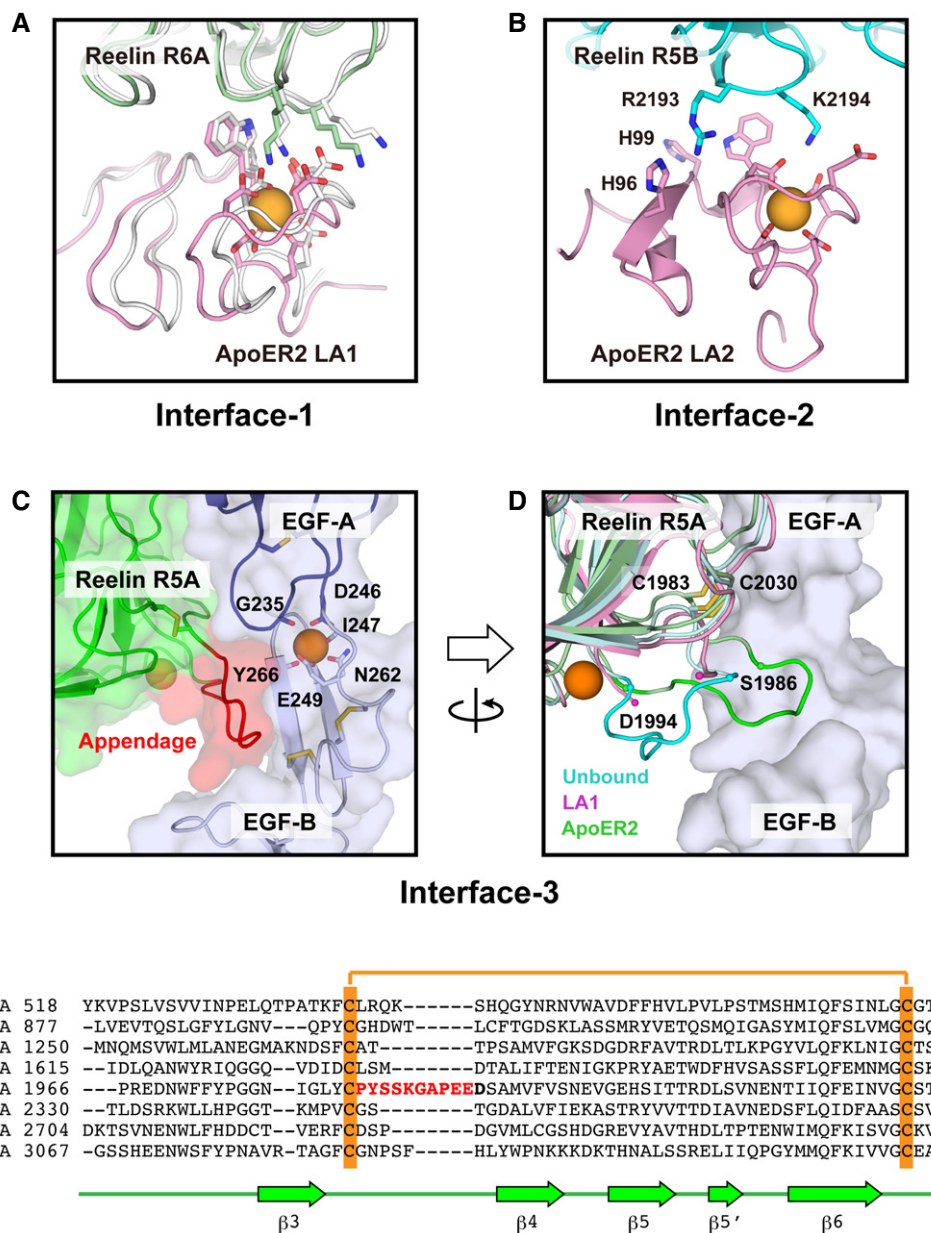


Figure 3. Three binding interfaces between ApoER2 ECD and reelin R56.

- A** Close-up view of Interface-1. The R6A subrepeat of reelin R56 and ApoER2 LA1 are shown in green and magenta, respectively. The side chains of the residues constituting the binding interface are shown as stick models while the calcium ion is indicated as an orange sphere. Crystal structure of reelin R56 in complex with LA1 (white; PDB code: 3A7Q) superposed onto R6A. Relative arrangement of R6A and LA1 is essentially consistent between the ApoER2 ECD:R56 and LA1:R56 complexes.
- B** Close-up view of Interface-2. In addition to K2194, R2193 on reelin R5B (cyan) seems to be involved in the interaction with ApoER2 LA2 (magenta). LA2 possesses two histidine residues, H96 and H99, close to the acidic cluster coordinating a calcium ion (orange sphere).
- C** Close-up view of Interface-3. The ribbon models of EGF-A (dark blue), EGF-B (light blue) and reelin R5A (green) are shown with transparent surface. The appendage-like loop of R5A is highlighted in red. Interface-3 is maintained through shape complementarity between the appendage-like loop and the concave surface of EGF-AB. As highlighted with the stick model, both of EGF-A and EGF-B provide for the residues coordinating a calcium ion (orange sphere).
- D** Comparison of conformation in the appendage-like loop region. The conformation of the loop is significantly different between the three available crystal structures, unbound R56 (cyan), in complex with ApoER2 LA1 (magenta), and in complex with ApoER2 ECD (green), whereas the base of the loop is fixed by a disulfide bond (stick model) and a calcium ion (orange sphere). The loop region between S1986 and D1994 is highlighted in dark color while the rest part of R5A is shown in light color in each reelin R5A model. The structure of ApoER2 EGF-AB is shown as a blue surface model.
- E** Sequence alignment of mouse reelin repeats around the appendage-like loop of reelin R5A. The loop between the β3 and β4 strands in R5A is obviously longer in comparison with the seven other reelin repeats. The region highlighted in red was substituted to a GS3 linker, and the mutant was subjected to SPR analysis (see Fig 4). The conserved cysteine pair that forms a disulfide bond is indicated in orange. The secondary structure of R5A was displayed below the alignment.

Examination of the interaction between reelin R5B and ApoER2 LA2

To examine the reliability of the model assignment and the contribution of Interface-2 to the complex stabilization, we introduced mutations to the binding site identified on reelin R5B. Based on the structural model, it seems that R2193, in addition to K2194, contributes to the specific interaction with the acidic residue cluster (Fig 3B). Supporting this conclusion, involvement of an analogous secondary basic residue has been frequently observed in the interaction of other LA–ligand pairs as well [16]. To abolish the putative interaction with LA2, the reelin R56 double-mutant R2193A/K2194A was constructed and subjected to SPR analysis. Consequently, this mutant showed a 10-fold drop in the binding affinity for the ApoER2 ECD wild type ($K_D = 1.6 \times 10^{-7}$ M; Fig 4A, Table 2). Obviously, the response curve dropped rapidly after the end of injection, indicating a faster dissociation of the R56 mutant compared with the wild type. This mutational effect is more likely explained by a change in interface affinity than by a change in tertiary conformation as the R2193A/K2194A R56 fragment and wild type R56 have similar hydrodynamic properties and thermal stabilities in analytical gel filtration and a thermal shift assay, respectively (Fig EV3).

Unique among the four LA modules in this ApoER2 splicing variant, LA2 contains two histidine residues (His-96 and His-99) on the binding surface (Figs 3B and EV1B). Protonation of histidine side chains under acidic conditions would be expected to disrupt the interaction with R2193 and K2194 on R5B due to electrostatic repulsion. We therefore constructed two ApoER2 ECD mutants, H96K/H99K and H96A/H99A, to test whether these two histidine residues act as a pH sensor. The H96K/H99K mutant mimics the protonated state of the histidine residues under acidic conditions while H96A/H99A abolishes electrostatic repulsion due to protonation. In fact, the dissociation constant between ApoER2 ECD and reelin R56 increased to 4.5×10^{-8} M by the mutation H96K/H99K under neutral pH conditions (Fig 4B, Table 2) while the reduction in the dissociation constant was observed for H96A/H99A under the same condition (8.0×10^{-9} M; Fig 4D, Table 2). Furthermore, the H96A/H99A mutation stabilized the interaction even under acidic pH conditions ($K_D = 1.2 \times 10^{-7}$ M; Fig 4E, Table 2) whereas the dissociation constant for H96K/H99K ($K_D = 4.9 \times 10^{-7}$ M; Fig 4C, Table 2) was comparable to that for the ApoER2 ECD wild type under neutral pH conditions as described above ($K_D = 4.1 \times 10^{-7}$ M; Table 1).

Dissecting the contribution to affinity from structural elements in the interface between reelin R5A and ApoER2 EGF-AB

Further inspection of the complex structure revealed an intimate intermolecular interaction between R5A and EGF-AB (referred to as Interface-3). A prominent feature of the interface on R5A is an appendage-like loop region (Cys-1983 to Asp-1994) formed between the $\beta 3$ and $\beta 4$ strands (Fig 3C). The loop fits into the concaved surface formed between EGF-A and EGF-B. A characteristic pair of cysteines is present to form a disulfide bond in all of the reelin repeats (Fig 3E), and Cys-1983 forms a disulfide bond with Cys-2030 in R5. Asp-1994 is located just upstream of the calcium-binding site, which is also a characteristic structural element of the subrepeats. Interestingly, the insertion between the $\beta 3$ and $\beta 4$ strands in R5A is exceptionally long compared to those in the other subrepeats A (Fig 3E). In addition, the conformation of this $\beta 3$ – $\beta 4$ loop differs between the three crystal structures of R56 that we have determined so far [30,31] (Fig 3D). In the structure of R56 alone, the loop region compactly packs against the surface of R5A. In the R56:LA1 complex, the loop appears to protrude out from R5A in an extended conformation. This conformation is consistent with the electron density in the present complex structure, although the model was not unambiguously assigned in this region due to disorder. While binding to EGF-AB may stabilize an alternate conformation of the loop, we were surprised to learn that it does not greatly contribute to affinity of the interface. In fact, the binding affinity did not change significantly when the appendage loop (Pro-1984 to Glu-1993) was replaced with a flexible linker composed of three repeats of glycine and serine ($K_D = 1.3 \times 10^{-8}$ M; Fig 4F, Table 2). It is possible that this negligible contribution is the result of an enthalpy–entropy tradeoff in the ordering of the loop in the wild-type interface.

Another minimal perturbation considering the central position of calcium ions in Interface-3, we hypothesized that this interface should also be sensitive to calcium depletion during endocytosis. EGF-A and EGF-B are classified as the calcium-binding EGF, and the calcium ion bound to EGF-B is located at the center of concaved surface. Although the influence of calcium depletion has not been studied for ApoER2, we hypothesized that eliminating calcium from our binding experiments would have a particularly strong effect on Interface-3. It has been reported for LDLR that the corresponding calcium ion dissociates from EGF-B under low calcium conditions even at neutral pH [36], while calcium ions seem to be more tightly bound to the LA modules under the same condition [37,38]. Therefore, we presumed from considerations of

Figure 4. Steady-state analysis of SPR data #2: Binding analysis targeted to Interface-2 and -3.

A representative result from triplicate SPR measurements is plotted for each condition.

- A Binding analysis between wild type ApoER2 and the reelin R56 R2193A/K2194A mutant. SPR analysis indicated that the mutations lead to a significant drop in the binding affinity for ApoER2 ECD at pH 7.5.
- B–E Mutations to H96/H99 of LA2. Binding analysis between ApoER2 ECD H96K/H99K and wild type reelin R56 at pH 7.5 (B) and 5.5 (C). H96K/H99K mimics the protonated state of ApoER2 ECD. Binding analysis between ApoER2 ECD H96A/H99A and wild type reelin R56 at pH 7.5 (D) and 5.5 (E). H96A/H99A abolishes protonation-dependent electrostatic repulsion.
- F Replacement of the appendage-like loop to three repeats of a glycine and serine (GS3) linker. The binding affinity of the GS3 linker mutant is consistent with that of the reelin R56 wild type.
- G SPR measurement between wild type ApoER2 ECD and wild type reelin R56 under low calcium conditions (Ca^{2+} : 3 μM). The overlaid sensorgrams and the result of curve fitting from steady-state affinity analysis are shown as in Fig 1.

Source data are available online for this figure.

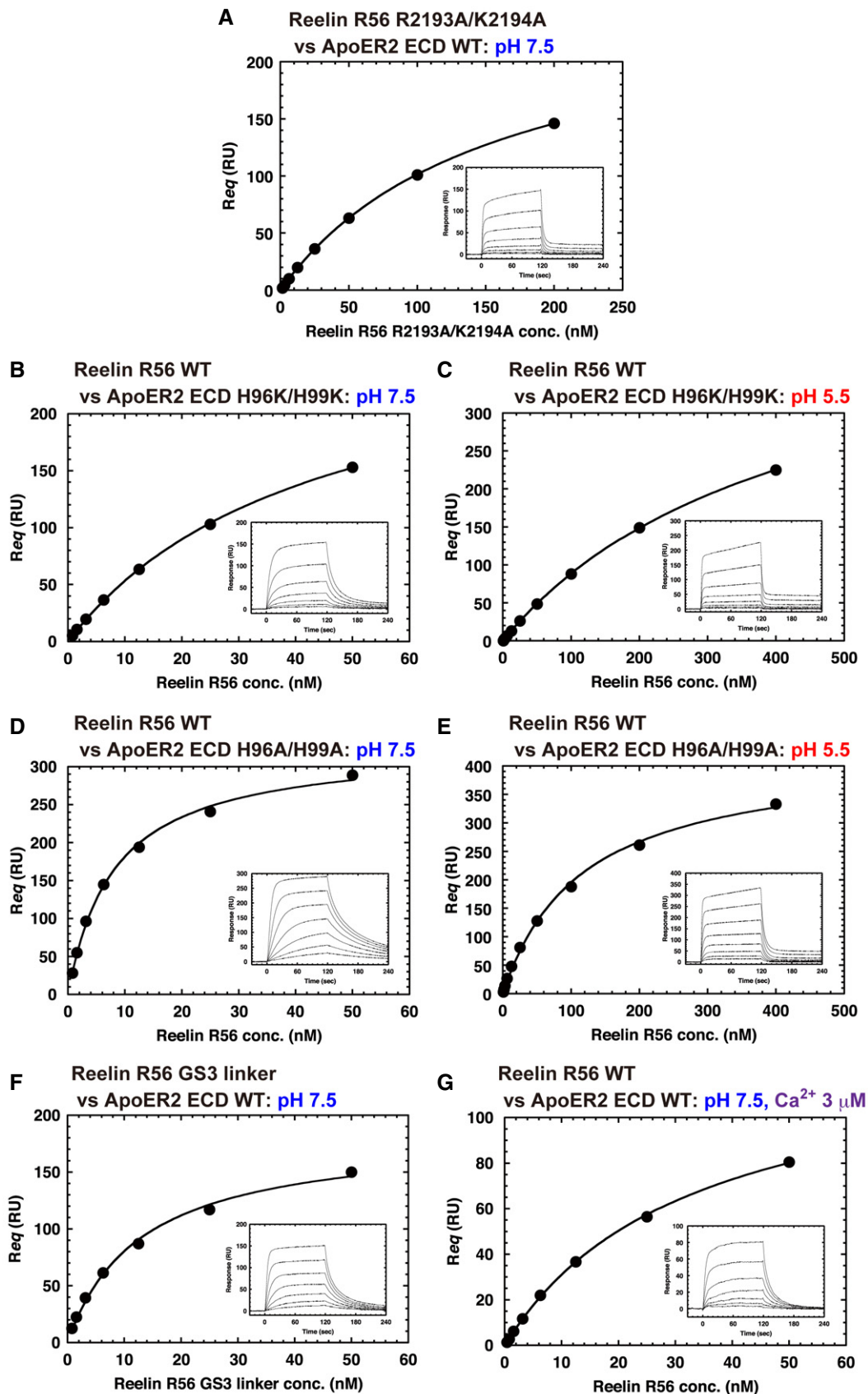


Figure 4.

Table 2. Summary of SPR analysis #2: Binding analysis targeted to Interface-2 and -3.

Analyte (reelin R56)	Ligand (ApoER2 ECD)	pH	Ca ²⁺ conc.	K _D (M) ^a	P-value
R2193A/K2194A	Wild type	7.5	2 mM	(1.6 ± 0.2) × 10 ⁻⁷	0.00460 ^b
Wild type	H96K/H99K/LA2	7.5	2 mM	(4.5 ± 0.2) × 10 ⁻⁸	0.00001 ^b
		5.5	2 mM	(4.9 ± 0.5) × 10 ⁻⁷	
Wild type	H96A/H99A/LA2	7.5	2 mM	(8.0 ± 0.2) × 10 ⁻⁹	0.00034 ^b
		5.5	2 mM	(1.2 ± 0.1) × 10 ⁻⁷	0.00006 ^c
GS3 linker	Wild type	7.5	2 mM	(1.3 ± 0.0) × 10 ⁻⁸	
Wild type	Wild type	7.5	3 μM	(3.3 ± 0.6) × 10 ⁻⁸	0.00430 ^b

^aEach K_D value represents the mean of triplicate SPR measurements with standard deviation. Processing of the sensorgram and curve fitting of affinity analysis were performed separately in the triplicate experiments, and the three obtained K_D values were used to calculate the mean, standard deviation, and P-value.

^bThe difference of the K_D value compared with that calculated for the interaction between reelin R56 wild type versus ApoER2 ECD wild type at pH 7.5 (see Table 1) is statistically significant with the indicated P-value, which is calculated by the unpaired two-tailed t-test.

^cThe difference of the K_D value compared with that calculated for the interaction between reelin R56 wild type versus ApoER2 ECD wild type at pH 5.5 (see Table 1) is statistically significant with the indicated P-value, which is calculated by the unpaired two-tailed t-test.

conserved sequence and function that the ApoER2 EGF-B domain is also likely to release the calcium ion under low calcium conditions, resulting in a considerable conformational change of the concaved surface. Nevertheless, the dissociation constant slightly increased from 1.2 × 10⁻⁸ M to 3.3 × 10⁻⁸ M (Fig 4G, Table 2) when the calcium concentration was lowered from 2 mM to 3 μM in the SPR analysis. Although the influence of calcium depletion would not be limited to a structural change of the concaved surface, the above result is consistent with our conclusion from mutation of the appendage loop that the contribution of Interface-3 to complex stabilization is marginal.

Discussion

In the present study, we have discovered that the LA2 module of ApoER2 provides an auxiliary binding interface for the reelin R56 fragment, supplementing the known high-affinity interface in LA1. In the crystallographic analysis, we located the LA2 module near the bottom face of reelin R5B, where the putative ligand-binding surface of LA2 recognizes two basic residues on R5B (R2193 and K2194) by the ligand-binding mechanism canonical to the LA module. In accordance with this, we observed through SPR analysis that the introduction of a salt bridge-disrupting mutation (E107Q) to LA2 slightly destabilized the complex by a roughly threefold change in K_D. Furthermore, the more severe R2193A/K2194A double mutation in R56 exhibited a significant 10-fold further increase in the dissociation constant of the complex as compared with the R56 wild type interaction.

Based on additional mutational analyses, we presume Interface-2 also plays a pivotal role in the ligand release process during endocytosis due to pH-sensitive histidines that are unique to Interface-2 among the interfaces between R56 and ApoER2. Our SPR analysis has shown that the binding affinity of the entire ApoER2 ECD:reelin R56 complex affinity is adversely affected by an acidic pH shift. Substitution of the two histidines to lysines destabilized the complex even under the neutral pH conditions whereas the substitution to alanines reduced the sensitivity to pH shift and stabilized the complex at acidic pH. The side chains of these two histidines are likely deprotonated in the crystal structure of ApoER2 ECD:reelin

R56 complex that was obtained at pH 7.5, enabling LA2 to interact with the positively charged surface of R5B.

Another important finding from the present structure determination is that the ectodomain of ApoER2 does not assume the extended conformation when it binds with reelin R56 under neutral pH conditions (Fig 5). This contradicts the general expectation that the extended conformation is necessarily the binding-active conformation in LDLR homologues. With respect to the position of the EGF-AB, the conformation of reelin R56 complexed ApoER2 is rather similar to the contracted-closed conformation of unbound LDLR under acidic conditions (Fig 5A and D). In our structure, the EGF-AB unit protrudes from the side of blades 5 and 6 of the YWTD β-propeller (Fig 5B and E), whereas EGF-AB of the LDLR:PCSK9 complex is located on the side of blades 1 and 2 in the extended conformation under neutral pH conditions (Fig 5C and F). These observations conform to the notion that the receptor in the open conformation where the LA modules are liberated from the YWTD domain is flexible due to the mobility of the EGF-AB unit, and indicate the presence of metastable conformation that is neither extended nor contracted-closed. We therefore defined the structure of the ApoER2 ectodomain with reelin R56 as a contracted-open conformation where the LA modules are open to the ligand but are positioned close to the top face of the YWTD domain. It seems that the formation of the contracted-open conformation is permitted by the presence of Interface-3 between EGF-AB and R6A. Without this interaction, the LA1 and LA2 modules, which, respectively, interact with basic residues of reelin R56 in a specific manner, cannot be located in proximity to the top face of YWTD. It was presumed that the receptor on the cell surface can explore a large conformational space, without interactions between the LA modules and YWTD domain, to capture the ligand. Our results, however, raised the possibility that ApoER2 has a preference for the contracted-open conformation after it binds with the ligand although the structure of ApoER2 ectodomain will be influenced to some degree by crystal lattice forces. The structural unit containing a YWTD flanked by two EGF modules (EGF-YWTD-EGF) occurs widely in the LDLR family members other than the LDLR close homologues. Interestingly, the N-terminal (incoming) EGF is located either between the blades 1 and 2, or between the blades 5 and 6 in all of the known crystal structures containing the EGF-YWTD-EGF unit, whereas the

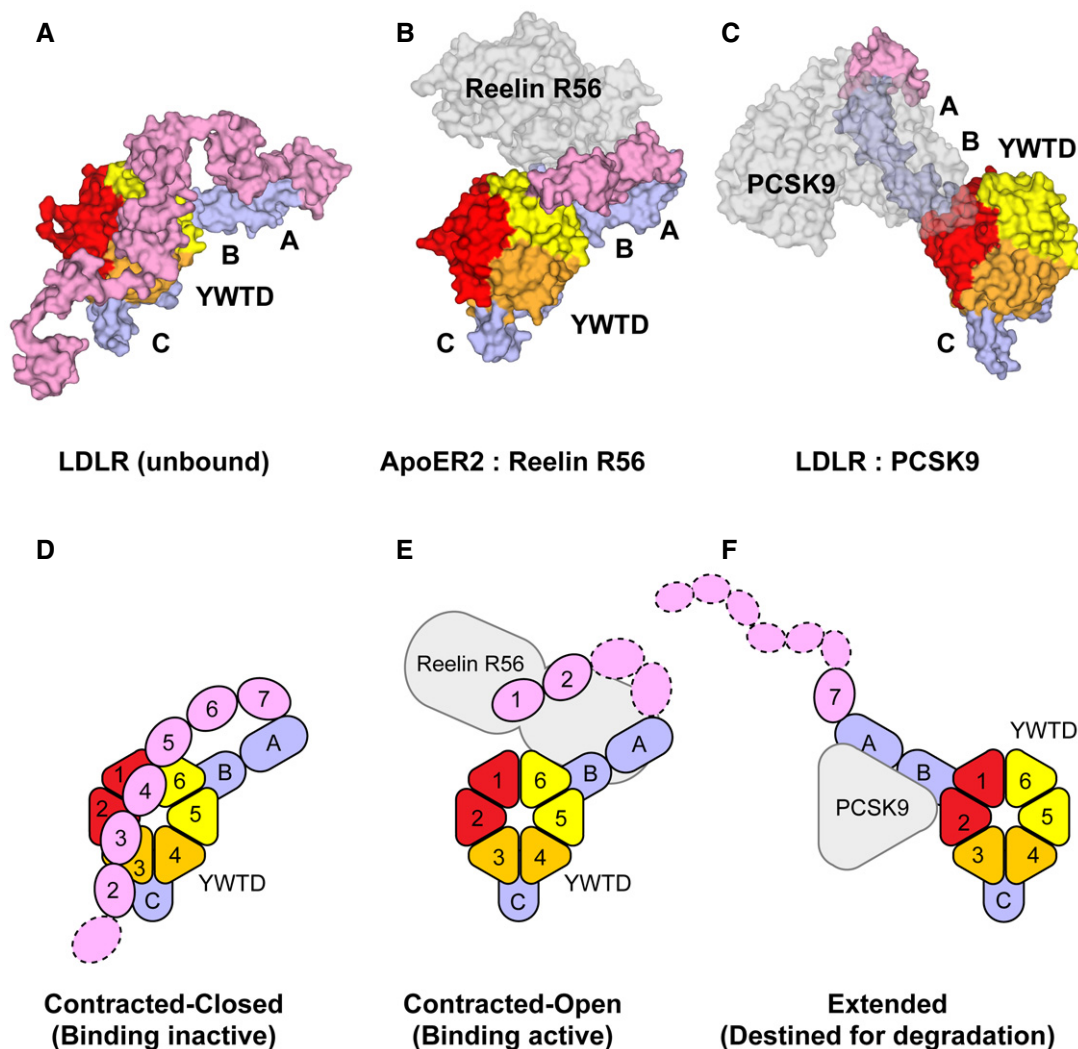


Figure 5. Conformation of the ectodomains of LDLR and ApoER2.

A–C Surface models viewed from the top face of the YWTD β -propeller.

D–F Diagram of the domain arrangement. For clarity, the six blades of the YWTD β -propeller are colored differently. The relative orientation of the EGF-AB unit against the YWTD β -propeller is completely different between unbound LDLR under acidic pH and that in complex with PCSK9 at the neutral pH, which causes the contracted-closed and extended conformations of the ectodomain, respectively. ApoER2 in complex with reelin R56 at the neutral pH assumes a contracted-open conformation similar to that of unbound LDLR but with a binding-active LA repeat conformation.

C-terminal (exiting) EGF is always located between the blades 3 and 4 (Fig EV4). We therefore presume that the arrangement of EGF-B unit against YWTD in the present ApoER2 structure is not a randomly chosen state out of numerous conformations, but reflects one of the two distinct metastable conformations of this receptor.

The structural features of the ApoER2 ECD:reelin R56 complex are also consistent with a common mechanism between ApoER2 and LDLR for the final process of ligand release. It has been reported in the crystallographic analysis of the full-length LDLR ectodomain that the contracted-closed conformation is mediated by the intramolecular interactions between the top face of the YWTD domain and the LA repeats, where the interaction via the LA4 module is dominant (Fig 6A and B). In LDLR, LA4 interacts with the side chain of K560 in the YWTD domain in a similar manner to the canonical ligand-binding mode of the LA modules. The YWTD

domain contains two histidines (H562 and H586) close to K560, and the protonation of these residues is thought to enhance the affinity between LA4 and YWTD under acidic conditions. In the above-discussed Interface-2 of the ApoER2 ECD:reelin R56 complex, the protonation of histidine residues in LA2 was expected to destabilize the interactions with the basic residues of R5B. In contrast, the protonated histidine residues of YWTD should stabilize the interactions with the LA4 module as they can form salt bridges with the acidic residues of LA4. In fact, it is also known that histidine mutations, such as H562Y, cause FH, likely because it reduces the release activity of LDL [39,40], suggesting the importance of the contracted-closed conformation for ligand release through a competitive inhibition mechanism. The corresponding lysine and two histidine residues are conserved on the top face of the ApoER2 YWTD domain and can constitute a putative intramolecular binding

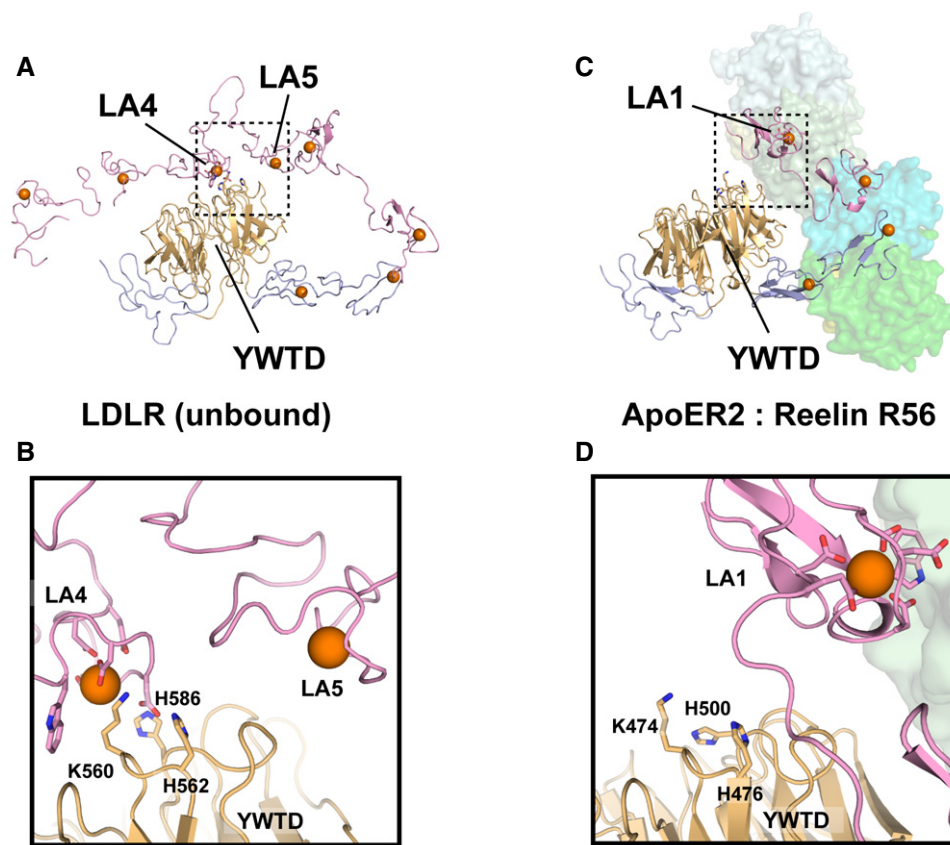


Figure 6. Putative intramolecular binding interface on the YWTD β -propeller.

- A The contracted-closed conformation of unbound LDLR is maintained through the interaction between the LA modules (magenta) and the YWTD domain (light orange). Calcium ions are shown as orange spheres.
- B Close-up view of the region indicated with dotted box in (A). Consistent with the canonical ligand-binding mode, K560 of YWTD is accommodated in the putative ligand-binding site of LA4. Protonated H562 and H586 seem to contribute to stabilization through electrostatic interactions with the acidic residues of LA4.
- C ApoER2 in complex with reelin R56 (surface model) assumes the contracted-open conformation where none of the LA modules make direct contact with YWTD.
- D Close-up view of the region indicated with dotted box in (C). ApoER2 YWTD (orange) also possesses the residues constituting the putative interface for the LA modules (magenta), that is, K474, H476, and H500 (stick). Based on the structure, LA1, which tightly interacts with the bottom face of reelin R6A (transparent surface), is closest to the putative interface on YWTD and seems to be ready for the partner exchange after dissociation from reelin R56.

interface (Fig 6C and D). Among the four LA modules in ApoER2, LA1 is the most proximal to this putative interface in the ApoER2 ECD:reelin R56 complex. Hence, there is a possibility that LA1 forms an intramolecular interaction with the putative interface on YWTD when the entire ApoER2:reelin complex is destabilized and LA1 dissociates from the bottom face of R6A after endocytosis. Such a partner exchange for the LA1 module should be the final step in the ligand release process. We postulate here that the reduction in the binding affinity of ApoER2 for reelin R56 under acidic pH is mainly derived from the electrostatic repulsion at Interface-2. Nevertheless, the increase in the dissociation constant under low pH was much larger than that arising from the H96K/H99K mutation on LA2, which mimics the pH-titrated disruption of Interface-2. The intramolecular interaction between LA1 and YWTD under acidic conditions, if it occurs, would sequester LA1 from interaction with reelin R56, decreasing the apparent association constant and the observed affinity. Further studies are required to address the issues of whether or not the contracted-closed conformation is formed through LA1, or any other LA modules, and whether or not it

promotes ligand release through a competitive inhibition mechanism in this splicing variant of ApoER2.

The present study again raises the importance of structural change from the extended to the contracted-closed conformation in receptor recycling. It has been hypothesized that the extended conformation observed in the LDLR:PCSK9 complex reflects a “recycling-inhibited” state, in which PCSK9 prevents the receptor from changing to the contracted-closed conformation [20]. The LDLR:PCSK9 complex is maintained by multiple interfaces where the YWTD domain as well as the EGF-A module serves as the binding sites for PCSK9. In fact, it has been shown that disruption of the extended conformation by mutation leads to a reduction in binding affinity for PCSK9, indicating the importance of proper positioning of the respective binding interfaces in the complex. In contrast, our present study revealed that ApoER2 can bind with its ligand, reelin R56, in the contracted-open conformation. Although disordered regions in the electron density demonstrate that the ApoER2 ectodomain remains flexible to a significant degree even after binding with reelin, it is suggested that the ligand binding guides the receptor to

adopt the conformation that can readily change to the contracted-closed conformation after the pH-titrated ligand dissociation. These observations raised the possibility that the ectodomain conformation correlates with the receptor fate in LDLR and its homologues. In other words, a contracted-open conformation leads to receptor recycling and an extended conformation leads to receptor degradation.

In conclusion, we first discovered, based on mutagenesis, the presence of an auxiliary low-affinity binding interface between ApoER2 and the signaling-competent R56 fragment of reelin. Subsequently, we succeeded in determining the crystal structure of the

full-length ectodomain of ApoER2 in complex with reelin R56. Our present structure demonstrates that ApoER2 assumes a contracted-open conformation when it binds with its ligand, in contrast to the previously reported extended conformation of LDLR in complex with PCSK9. The contracted-open conformation is maintained by multiple binding interfaces between the receptor and ligand, and the binding affinity of the auxiliary interface seems to be weakened mainly by the pH shift during internalization. Although the structure of unbound ApoER2 has not yet been determined, the conservation of the basic patch on the YWTD domain indicates that ApoER2

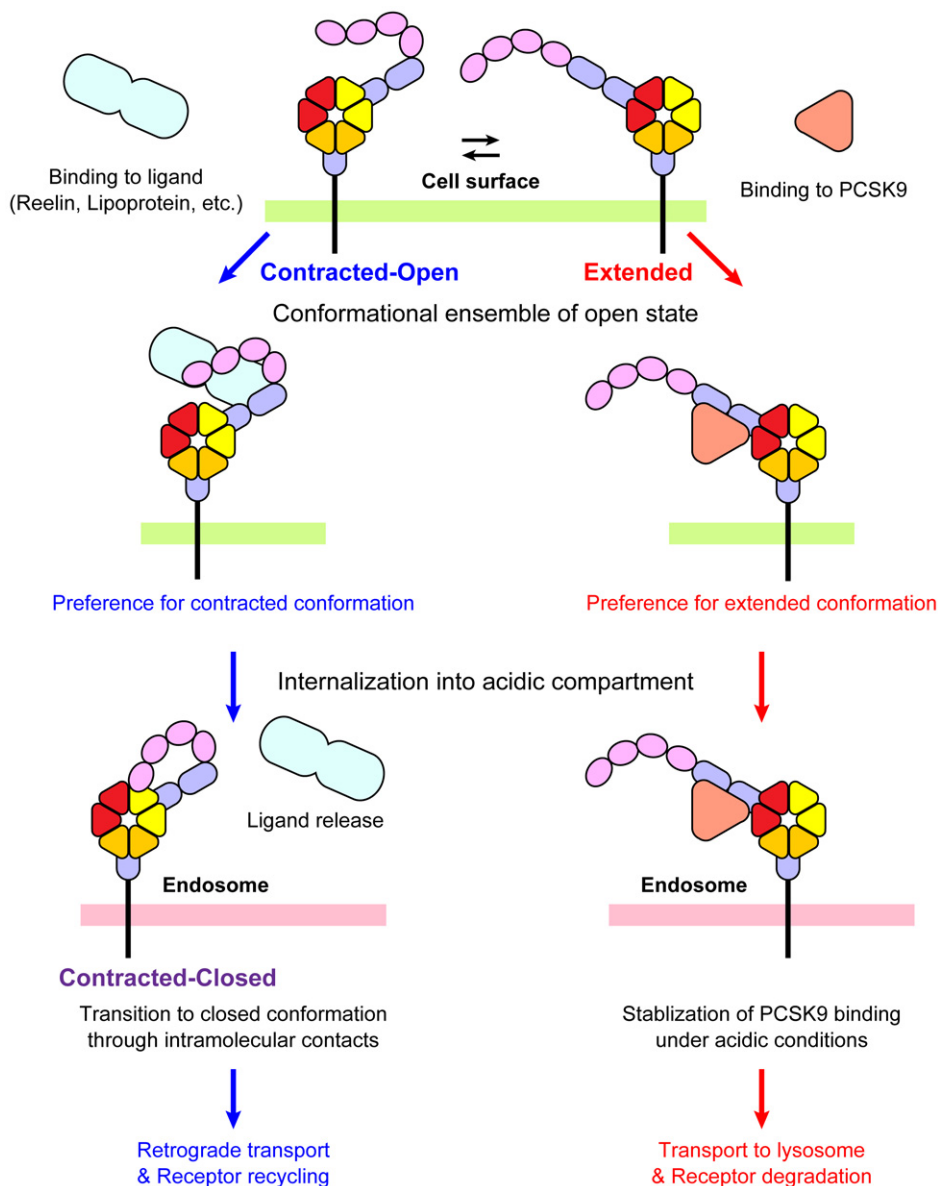


Figure 7. Mechanistic model for receptor recycling and degradation in ApoER2.

The present structural analysis suggests that ApoER2 in complex with its ligands, such as reelin R56, has a preference for adopting the contracted-open conformation although it should exist in equilibrium between the contracted-open and extended conformations at the cell surface. After the receptor:ligand complex is internalized through endocytosis, the binding affinity decreases due to the pH shift in the endosomal compartment. In such an environment, ApoER2 is also expected to assume a contracted-closed conformation to release the ligand, as LDLR does. Subsequently, the receptor is transported back to the cell surface and recycled. In contrast, the previous crystallographic and mutational analyses have indicated that LDLR in complex with PCSK9 has a preference for the extended conformation. It is also known that the binding affinity for PCSK9 is enhanced under acidic conditions. The LDLR:PCSK9 complex is therefore stabilized after internalization and is transported to the lysosome for degradation.

could be capable of adopting the contracted-closed conformation through intramolecular contacts between the LA modules and YWTD domain after endocytosis. Based on the structural data from the present study, we propose a mechanistic model for the ligand uptake and receptor recycling in ApoER2 (Fig 7). Although the number of LA repeats is different between LDLR and the splicing variant of ApoER2 studied in the current work, our ApoER2 structure in complex with reelin R56 is expected to serve as a structural basis for analyzing the pH-dependent ligand uptake mechanism conserved among the LDLR family members. Profound understanding of the mechanism should also contribute to development of a strategy for regulating LDL uptake and receptor recycling, which would further lead to the development of future therapeutic strategies for FH.

Materials and Methods

Expression of biotinylated ApoER2 ECD for surface plasmon resonance analysis

For immobilization on the sensor chip surface, human ApoER2 ECD was fused to a biotin acceptor sequence (ApoER2 ECD-BAS), and then biotinylated by co-expression with biotin ligase from *E. coli* (BirA) as described previously [41]. More precisely, the gene for ApoER2 ECD-BAS was cloned into the pSGHV0 vector [42] to produce it with N-terminally fused human growth hormone (hGH) plus an octahistidine (His₈) tag and the tobacco etch virus (TEV) protease consensus sequence. The modified BirA construct (sBirA-KDEL) contains the N-terminal signal peptide of bovine prolactin for translocation and a C-terminal ER retention signal for localization. The mutations to disrupt interface salt bridges were introduced to the LA modules of ApoER2 ECD-BAS according to the QuikChange protocol (Agilent Technologies). The constructed plasmids encoding ApoER2 ECD-BAS and sBirA-KDEL were co-transfected into HEK-293T cells using polyethylene imine (PEI), then cultured for 3–4 days in complete DMEM containing 10% fetal bovine serum and 100 μM D-biotin. The harvested cell culture supernatant was clarified by centrifugation and filtration, neutralized by adding 1.0 M Tris-Cl (pH 8.0) to a final concentration of 10 mM, and then incubated with Ni-NTA agarose beads. After washing beads with 20 mM HEPES-Na (pH 7.5), 300 mM NaCl, the proteins were eluted with 20 mM HEPES-Na (pH 7.5), 300 mM NaCl, and 250 mM imidazole. N-terminally hexahistidine-tagged TEV protease (His₆-TEV) was added to the elution fraction to cleave off the N-terminal hGH-His₈ portion, and then the fraction was dialyzed against 20 mM HEPES-Na (pH 7.5), and 300 mM NaCl overnight at 4°C. The hGH-His₈ portion and His₆-TEV were removed by passing the fraction through Ni-NTA agarose. Finally, the flow-through fraction containing ApoER2 ECD-BAS was collected and concentrated by ultrafiltration using a Spin-X[®] UF Concentrator with a molecular weight cutoff of 30 kDa (Corning).

Expression and purification of reelin R56 for surface plasmon resonance analysis

Recombinant mouse reelin R56 protein fused to a TEV protease recognition site and a PA tag at the C-terminus was transiently

expressed in HEK293S GnTI-cells [43]. PA-tagged reelin R56 was purified from culture supernatant using NZ-1-immobilized Sepharose as described previously [44]. The C-terminal PA tag was removed by TEV protease treatment, and the reelin R56 fragment was further purified by gel filtration on HiLoad 16/60 Superdex 200 prep grade (GE Healthcare) equilibrated with 20 mM HEPES-Na (pH 7.5) and 150 mM NaCl. The fractions containing reelin R56 were pooled and concentrated by ultrafiltration. In addition, the double mutation R2193A/K2194A was introduced into the reelin R56 construct using the QuikChange protocol while the appendage loop-replaced mutant was constructed by an inverse PCR strategy. These mutants were also expressed and purified according to the same protocol as that for the wild type.

Surface plasmon resonance analysis

Surface plasmon resonance was performed with a Biacore 2000 instrument (GE Healthcare) at 25°C in 20 mM HEPES-Na (pH 7.5), 150 mM NaCl, 2 mM CaCl₂, and 0.005% (wt./vol.) Surfactant P20. Biotinylated ApoER2 ECD-BAS fragments were diluted in running buffer, and then immobilized as the ligand on a Sensor Chip SA up to an average of 550 resonance units (RU), according to the manufacturer's protocol. Sensorgrams were collected by injecting various concentrations of wild type or mutant reelin R56 fragments as the analytes. For regeneration, the sensor chip was washed with 20 mM HEPES-Na (pH7.5), 1 M NaCl, and 20 mM EDTA after each run. The sensorgrams were corrected for bulk refractive index errors using a mock flow cell containing only pre-coupled SA. Dissociation constants (K_D) were calculated using BIAevaluation with affinity analysis. The binding response after 120 sec injection at a flow rate of 30 μl/min was recorded as the response at equilibrium (R_{eq}). The R_{eq} value was plotted against the concentration of analyte (C) and subjected to least-square fitting to the following equation: $R_{eq} = K_A \times C \times R_{max} / (1 + K_A \times C)$ where $K_A = 1 / K_D$ and R_{max} is the theoretical maximum binding response. Under low pH conditions, measurement was performed using 20 mM MES-Na (pH5.5), 150 mM NaCl, 2 mM CaCl₂, and 0.005% (wt./vol.) Surfactant P20. The K_D value in each condition was estimated as the mean of triplicate measurements with the standard deviation. The results of SPR analysis were summarized in Tables 1 and 2.

Expression and purification of ApoER2 ECD for crystallization

To produce the ApoER2 ECD fragment, CHO lec 3.2.8.1 cells [45] were transfected with plasmid encoding ApoER2 ECD fused with hGH plus His₈ and a TEV recognition site at the N-terminus (hGH-ApoER2 ECD) [30] and selected for resistance against 1.5 mg/ml G418. The clone with the highest secretion levels was cultured in a roller bottle (Corning). The culture supernatant was collected in a dialysis tube and concentrated with Aquacide II (Merck Millipore). The hGH-ApoER2 ECD was purified from the concentrated culture supernatant with Ni-NTA agarose. After washing the beads with 20 mM Tris-Cl (pH 8.0), 300 mM NaCl, and 20 mM imidazole, the proteins were eluted with 20 mM Tris-Cl (pH 8.0), 300 mM NaCl, and 250 mM imidazole. The fusion proteins were treated with His₆-TEV protease to release the hGH plus His₈ tag. TEV protease and hGH-His₈ were removed by a second round of Ni-NTA agarose chromatography. The ApoER2 ECD fragment was

further purified by loading onto anion-exchange chromatography on a MonoQ 5/50GL column (GE Healthcare) equilibrated with 20 mM Tris-Cl (pH 8.0), and 1 mM CaCl₂ and eluting over a linear gradient from 0 to 400 mM NaCl over a 20-column volume at a flow rate of 1 ml/min.

Preparation of SeMet-substituted reelin R56

Previous work has described the stable transfectant of CHO lec 3.2.8.1 cells that expresses the reelin R56 fragment fused to an N-terminal signal sequence from mouse nidgen-1 and to a C-terminal TEV protease recognition site [30]. To prepare the selenomethionyl-substituted reelin R56, cells in culture flasks were washed with phosphate-buffered saline and incubated with methionine-free alpha-MEM (Cell Science & Technology Institute, Sendai, Japan), supplemented with 5% dialyzed fetal bovine serum (Invitrogen), 50 mg/l L-selenomethionine (SeMet) (Wako Chemical Co.). The media from the first 12–14 h of culture were discarded, and cells were incubated in fresh media supplemented with SeMet for 2–3 days. The SeMet-substituted reelin R56 was purified from the culture supernatants by ammonium sulfate precipitation and Ni-NTA agarose chromatography (QIAGEN). After washing the Ni-NTA agarose column with 20 mM Tris-Cl (pH 8.0), 300 mM NaCl, and 50 mM imidazole, the proteins were eluted with 20 mM Tris-Cl (pH 8.0), 300 mM NaCl, and 250 mM imidazole. The fractions containing the reelin R56 fragment were pooled, treated with His₆-TEV protease at room temperature, and passed through a Ni-NTA agarose column to remove the cleaved tag and enzyme. Further purification was carried out by gel filtration chromatography on a Superdex 200 10/300 GL column (GE Healthcare) equilibrated with 20 mM Tris-Cl (pH 7.5), 150 mM NaCl, and 1 mM CaCl₂, at a flow rate of 0.5 ml/min.

Preparation of the ApoER2 ECD:reelin R56 complex

Prior to crystallization of the ApoER2 ECD:SeMet-labeled reelin R56 complex, the optimal ratio of each component to form the complex was estimated by gel filtration chromatography. ApoER2 ECD and reelin R56 fragments purified as described above were mixed at various ratios and subjected to a Superdex 200 10/300 GL column equilibrated with 20 mM Tris-Cl (pH 7.5), 150 mM NaCl, and 2 mM CaCl₂. A mixture of reelin R56 and ApoER2 ECD at the ratio providing a single peak corresponding to their complex on the elution profile was used for crystallization. The protein concentration of the complex was estimated to be ~10 mg/ml using the molar extinction coefficients at 280 nm for ApoER2 ECD and reelin R56 [46].

Preparation of the ApoER2 LA12 fragment

The LA12 fragment was overexpressed as a glutathione S-transferase (GST) fusion protein in *E. coli* BL21 (DE3) where a His₈ tag and a TEV protease recognition site were incorporated between the GST and LA12 portions. *E. coli* cells were cultured at 37°C for 4 h after induction of protein expression with 1 mM isopropyl-β-D-thiogalactopyranoside and harvested as a pellet by centrifugation. Subsequently, the cells were resuspended and lysed by sonication in a buffer containing 10 mM Tris-Cl (pH 8.0), 300 mM NaCl, and

10 mM imidazole supplemented with 1 mM dithiothreitol. After removing the cell debris, the supernatant of the cell lysate was applied on a Ni-NTA agarose column (GE Healthcare). The bound fusion protein was washed with 10 mM Tris-Cl (pH 8.0), 300 mM NaCl, and 20 mM imidazole, and eluted with 10 mM Tris-Cl (pH 8.0), 300 mM NaCl, and 250 mM imidazole. Elution fractions containing the fusion protein were dialyzed against 20 mM Tris-Cl (pH 8.0) and 300 mM NaCl, and treated with His₆-TEV to cleave off the GST-His₈ portion. The TEV-treated fractions were passed through a Ni-NTA column again, and the LA12 fragment was collected as flow-through. Subsequently, the LA12 fragment was refolded by dialysis at 4°C against 50 mM Tris-Cl (pH 8.0), 10 mM CaCl₂, 2 mM L-cysteine, and 0.5 mM L-cystine according to the protocol reported previously [47]. The refolded LA12 fragment was applied to a MonoQ 5/50GL anion-exchange column (GE Healthcare) equilibrated with 20 mM Tris-Cl (pH 8.0) and 1 mM CaCl₂, and eluted on a linear gradient from 0 to 500 mM NaCl over a 20-column volume at a flow rate of 1.0 ml/min. The fractions containing the properly folded fragment were further purified on a Superdex 200 10/300GL gel filtration chromatography column (GE Healthcare) by an isocratic elution with 20 mM Tris-Cl (pH 8.0), 150 mM NaCl, and 2 mM CaCl₂ at a flow rate of 0.5 ml/min. The purified LA12 fragment was concentrated by ultrafiltration, and the protein concentration was estimated to be ~5.9 mg/ml according to the same method as described above.

Crystallization and data collection

Initial crystallization conditions were searched by random screening where 0.1 μl of the protein solution was mixed with the same volume of precipitant solution using a mosquito[®] (TTPLabtech), and equilibrated against 100 μl of the precipitant solution in the reservoir. For the ApoER2 ECD:reelin R56 complex, diffraction quality crystals were reproducibly obtained from a solution containing 11–12.5% (wt./vol.) PEG3350, 200–250 mM sodium thiocyanate, and 20 mM HEPES-Na (pH 7.5) after optimization. For the LA12 fragment, a single crystal obtained from the commercial screening kit, Wizard[™] I (Emerald BioStructures), was used for data collection. The composition of the reservoir is as follows: 20% (wt./vol.) PEG monomethylether 2000 and 100 mM Tris-Cl (pH 7.0). Prior to data collection, the crystals were soaked in cryoprotectant prepared by mixing the reservoir and ethylene glycol at a volume ratio of 4:1, and flash frozen in liquid nitrogen. For the complex, X-ray diffraction data were collected at Photon Factory (PF) BL-5A with an ADSC Quantum 315r CCD detector using the inverse beam mode to ensure the quality of anomalous signal. For the LA12 fragment, data collection was performed at PF BL-17A using an ADSC Quantum 315r CCD detector. The diffraction images were processed with XDS [48]. The diffraction intensities were then scaled and converted to structure factors with AIMLESS [49] and TRUNCATE [50] in the CCP4 program suite [51,52]. The data collection statistics are summarized in Table 3.

Structure determination of the ApoER2 LA12 fragment

The crystal structure of the LA12 fragment was solved by molecular replacement method using the program MOLREP [53]. Both of the LA1 and LA2 modules were successfully assigned by using the

Table 3. Data collection and refinement statistics in X-ray crystallographic analysis.

Molecular entities	Reelin R56: ApoER2 ECD	ApoER2 LA12
Data collection		
Space group	$P6_5$	$P2_12_12_1$
Cell dimensions		
a, b, c (Å)	205.95, 205.95, 169.84	31.16, 41.78, 55.06
α, β, γ (°)	90, 90, 120	90, 90, 90
No. of monomers or complexes/ a.s.u.	2	1
X-ray source	PF/BL-5A	PF/BL-17A
Wavelength (Å)	0.97904	1.00000
Resolution limits (Å)	49.5–3.20 (3.28–3.20)	41.8–1.90 (1.94–1.90)
No. of unique reflections	67,441 (4,551)	6,043 (372)
Completeness (%)	100 (100)	99.9 (100)
Redundancy	14.8 (14.6)	5.2 (5.3)
$\langle I/\sigma(I) \rangle$	16.4 (2.6)	9.5 (1.9)
R_{merge}^a	0.139 (1.051)	0.086 (0.855)
$CC_{1/2}$	0.997 (0.873)	0.995 (0.711)
Refinement		
Resolution limits (Å)	49.5–3.20 (3.28–3.20)	33.3–1.90 (1.95–1.90)
R_{work}^b	0.200 (0.260)	0.210 (0.315)
R_{free}^c	0.255 (0.310)	0.247 (0.282)
No. of non-H atoms	18,892	668
Protein/sugar/solvent	18,822 / 70 / 0	633 / 0 / 35
Averaged temperature factors (Å ²)	99.77	37.36
Protein/sugar/solvent	99.80 / 92.74 / –	37.05 / – / 43.00
RMSD from ideality		
Bond length (Å)/ bond angle (°)	0.006 / 1.18	0.012 / 1.67
Ramachandran plot (MolProbity)		
Favored/Outlier (%)	89.8 / 0.30	98.7 / 0

Values in parentheses are for highest resolution shell.

^a $R_{\text{merge}} = \sum_i \sum_j |I_i(h) - \langle I(h) \rangle| / \sum_i \sum_j I_i(h)$, where $I_i(h)$ is the i th measurement.

^b R_{work} is the crystallographic R -factor (R_{cryst}) for the working set used for the refinement. $R_{\text{cryst}} = \sum_h |F_{\text{obs}}(h) - F_{\text{calc}}(h)| / \sum_h |F_{\text{obs}}(h)|$, where $F_{\text{obs}}(h)$ and $F_{\text{calc}}(h)$ are the observed and calculated structure factors.

^c R_{free} is R_{cryst} calculated for the test set consisting of 5% of reflections excluded from the refinement.

ApoER2 LA1 structure (PDB code: 3A7Q) as the search model. Manual model fitting and refinement were performed using the programs COOT [54] and REFMAC5 [55], respectively. After several rounds of refinement, the crystallographic R -factor and free R -factor were reduced to 20.96 and 23.96%, respectively, at 1.9 Å resolution. The quality of the final model was validated using the program MolProbity [56]. 97.5% of the 79 amino acid residues in the model were located in the favored region, and no residues were assigned as the outliers.

Structure determination of the ApoER2 ECD:reelin R56 complex

The crystal structure of the ApoER2 ECD:reelin R56 complex was solved by the Se-SAD method. We identified the positions of Se atoms with the program HKL2MAP [57] coupled with SHELXC/D [58], and the phases were calculated and improved with SHARP/ autoSHARP [59,60]. Initial models for the respective modules were built by using the known structures. For the reelin R56 and ApoER2 LA1 pair, the crystal structure of their complex (PDB code: 3A7Q) was used as the initial model and fitted into the electron density. For the ApoER2 EGFP domain, the structure of the full-length LDLR ectodomain (PDB code: 1N7D) and the partial models (PDB codes: 1IJQ and 1HJ7) were used as the reference. Among the remaining three LA modules of ApoER2, LA3 and 7 were not modeled at all due to disorder. Although electron density for putative LA2 modules was weak, we were able to assign a plausible model using a procedure termed as constrained local real space search, as described in the next section. Manual model fitting and refinement were performed essentially as described above. The crystallographic R -factor and free R -factor were finally reduced to 18.46 and 25.60%, respectively, at 3.2 Å resolution. Among the 2,377 residues in the model, 89.6% were located in the favored region and only 0.3% were assigned as outliers.

Model assignment of the LA2 fragment by the constrained local real space search

In contrast to LA3 and LA7, electron density of putative LA2 module was definitely observed in the vicinity of LA1 module. However, due to weak density, any attempt to model LA2 module was failed including manual chain tracing and real space fragment search. Then, we performed the constrained local real space fragment search. The starting coordinates of LA2 were manually determined by locating high-resolution LA2 model at the center of the electron density blob of $2mF_o - DF_c$ map (Fig 2D). As LA2 is covalently linked to LA1 with a loop consisting of four residues, any candidates with the distance between the terminal residues larger than 3.7×5 Å were rejected. The candidates were evaluated by a scoring function S which evaluates electron density values at atomic coordinates; $S(\Delta x, \Delta y, \Delta z, \alpha, \beta, \gamma) = \sum_j \rho(R(\alpha, \beta, \gamma) \mathbf{r}_j + {}^t(\Delta x, \Delta y, \Delta z))$, where $\rho(\mathbf{r})$ is the linearly interpolated electron density value at \mathbf{r} , R is the rotation matrix, and ${}^t(\Delta x, \Delta y, \Delta z)$ is the translation vector. The sampling intervals for rotation and translation were 15° and 1 Å, respectively. The translation search was limited within ± 5 Å for each direction. This procedure was implemented as a C++ program using the Clipper library [61]. After rejecting any candidates that clashed with atoms of other domains, the candidate with the highest score S was selected as the solution (Fig EV2A and B). This procedure was independently applied to two copies of LA2 in the asymmetric unit, and consistent solutions were obtained. The linker between LA1 and LA2 was manually built using COOT. The whole model was subjected to restrained refinement using REFMAC5 with external structural restraints using high-resolution LA2 structure and a jelly-body refinement scheme [62]. The external structural restraints were prepared using ProSMART [63]. The real space correlation coefficient (RSCC) was evaluated for LA2 with $2mF_o - DF_c$ map using *phenix.get_cc_mtz_pdb* [64]. The local

RSCC after the refinement for two copies of LA2 was 0.677 and 0.649, respectively.

Analytical gel filtration

Analytical gel filtration was performed with an AKTApurifier instrument (GE Healthcare). 10 µg of purified wild type or mutant reelin R56 was applied to a Superdex 200 Increase 10/300 GL column (GE Healthcare) equilibrated with 20 mM HEPES-Na (pH7.5), 150 mM NaCl, and 2 mM CaCl₂. The theoretical molecular weight (Mw) was calculated using ExPasy ProtParam tool [65], and the estimated Mw was calculated using Gel Filtration Standard (Bio-Rad) supplemented with ferritin protein as a standard.

Thermal shift assay

Thermal shift assay was performed with a CFX96 Touch Real-Time PCR Detection System (Bio-Rad). For each wild type and mutant sample, 4 µl of 100 ng/µl reelin R56 was dispensed in 0.2-ml tubes and diluted with 15 µl of 20 mM HEPES-Na (pH7.5), 150 mM NaCl, and 2 mM CaCl₂. Subsequently, the measurement was started immediately after adding 1 µl of 150-fold diluted SYPRO Orange (Invitrogen) to the diluted protein solution. During the experiment, the temperature was increased from 25 to 85°C in 60 steps with a ramp rate of 0.1°C/s at each step.

Accession numbers

The atomic coordinates and structure factors of the ApoER2 ECD: reelin R56 complex and the ApoER2 LA12 fragment have been deposited in the Protein Data Bank with accession numbers of 5B4X and 5B4Y, respectively.

Expanded View for this article is available online.

Acknowledgements

We are grateful to the staff of beamlines BL-5A and 17A at Photon Factory (Tsukuba, Japan) for providing data collection facilities and support. We thank Samuel Thompson for editing the manuscript and Prof. Mitsuharu Hattori for useful discussion. This work was partly supported by the research grants from the Japan Society for the Promotion of Science (JSPS); the Grant-in-Aids for Scientific Research (A) No. 22247010 (to JT), the Grant-in-Aid for Young Scientists (B) No. 20770084 (to NY), and the Grant-in-Aid for JSPS Fellows No. 05J09821 (to NY), by the research grant from the Ministry of Education, Culture, Sports, Science and Technology (MEXT); the Grant-in-Aid for Scientific Research on Priority Areas No. 17082004 (to JT), by the research grant from Daiichi Sankyo Foundation of Life Science (to TN), and by the Platform Project for Supporting in Drug Discovery and Life Science Research (Platform for Drug Discovery, Informatics, and Structural Life Science) from the Ministry of Education, Culture, Sports, Science and Technology (MEXT), and Japan Agency for Medical Research and Development (AMED) (to MY, JT and TN). This work was performed partly under the Cooperative Research Program of Institute for Protein Research, Osaka University, CR-15-05.

Author contributions

JT and TN designed the study. HH, NY, and ST contributed the protein production and crystallization. HH, NY, and TN performed the crystallographic analysis. KY and MY developed the protocol of the constrained local real space

search. HH performed the SPR measurements and analyzed the results. HH, NY, KY, JT, and TN wrote the manuscript.

Conflict of interest

The authors declare that they have no conflict of interest.

References

1. Brown MS, Goldstein JL (1986) A receptor-mediated pathway for cholesterol homeostasis. *Science* 232: 34–47
2. Brown MS, Goldstein JL (1974) Expression of the familial hypercholesterolemia gene in heterozygotes: mechanism for a dominant disorder in man. *Science* 185: 61–63
3. Usifo E, Leigh SE, Whittall RA, Lench N, Taylor A, Yeats C, Orengo CA, Martin AC, Celli J, Humphries SE (2012) Low-density lipoprotein receptor gene familial hypercholesterolemia variant database: update and pathological assessment. *Ann Hum Genet* 76: 387–401
4. Yamamoto T, Davis CG, Brown MS, Schneider WJ, Casey ML, Goldstein JL, Russell DW (1984) The human LDL receptor: a cysteine-rich protein with multiple Alu sequences in its mRNA. *Cell* 39: 27–38
5. Südhof TC, Goldstein JL, Brown MS, Russell DW (1985) The LDL receptor gene: a mosaic of exons shared with different proteins. *Science* 228: 815–822
6. Jeon H, Blacklow SC (2005) Structure and physiologic function of the low-density lipoprotein receptor. *Annu Rev Biochem* 74: 535–562
7. Springer TA (1998) An extracellular beta-propeller module predicted in lipoprotein and scavenger receptors, tyrosine kinases, epidermal growth factor precursor, and extracellular matrix components. *J Mol Biol* 283: 837–862
8. Fass D, Blacklow S, Kim PS, Berger JM (1997) Molecular basis of familial hypercholesterolemia from structure of LDL receptor module. *Nature* 388: 691–693
9. North CL, Blacklow SC (2000) Solution structure of the sixth LDL-A module of the LDL receptor. *Biochemistry* 39: 2564–2571
10. Daly NL, Scanlon MJ, Djordjevic JT, Kroon PA, Smith R (1995) Three-dimensional structure of a cysteine-rich repeat from the low-density lipoprotein receptor. *Proc Natl Acad Sci USA* 92: 6334–6338
11. Daly NL, Djordjevic JT, Kroon PA, Smith R (1995) Three-dimensional structure of the second cysteine-rich repeat from the human low-density lipoprotein receptor. *Biochemistry* 34: 14474–14481
12. Clayton D, Brereton IM, Kroon PA, Smith R (2000) Three-dimensional NMR structure of the sixth ligand-binding module of the human LDL receptor: comparison of two adjacent modules with different ligand binding specificities. *FEBS Lett* 479: 118–122
13. Kurniawan ND, Atkins AR, Bieri S, Brown CJ, Brereton IM, Kroon PA, Smith R (2000) NMR structure of a concatamer of the first and second ligand-binding modules of the human low-density lipoprotein receptor. *Protein Sci* 9: 1282–1293
14. Huang W, Dolmer K, Gettins PG (1999) NMR solution structure of complement-like repeat CR8 from the low density lipoprotein receptor-related protein. *J Biol Chem* 274: 14130–14136
15. Russell DW, Brown MS, Goldstein JL (1989) Different combinations of cysteine-rich repeats mediate binding of low density lipoprotein receptor to two different proteins. *J Biol Chem* 264: 21682–21688
16. Fisher C, Beglova N, Blacklow SC (2006) Structure of an LDLR-RAP complex reveals a general mode for ligand recognition by lipoprotein receptors. *Mol Cell* 22: 277–283

17. Verdaguer N, Fita I, Reithmayer M, Moser R, Blaas D (2004) X-ray structure of a minor group human rhinovirus bound to a fragment of its cellular receptor protein. *Nat Struct Mol Biol* 11: 429–434
18. Zaiou M, Arnold KS, Newhouse YM, Innerarity TL, Weisgraber KH, Segall ML, Phillips MC, Lund-Katz S (2000) Apolipoprotein E₂-low density lipoprotein receptor interaction. Influences of basic residue and amphipathic alpha-helix organization in the ligand. *J Lipid Res* 41: 1087–1095
19. Rudenko G, Henry L, Henderson K, Ichtchenko K, Brown MS, Goldstein JL, Deisenhofer J (2002) Structure of the LDL receptor extracellular domain at endosomal pH. *Science* 298: 2353–2358
20. Lo Surdo P, Bottomley MJ, Calzetta A, Settembre EC, Cirillo A, Pandit S, Ni YG, Hubbard B, Sitlani A, Carfi A (2011) Mechanistic implications for LDL receptor degradation from the PCSK9/LDLR structure at neutral pH. *EMBO Rep* 12: 1300–1305
21. Li J, Tumanut C, Gavigan JA, Huang WJ, Hampton EN, Tumanut R, Suen KF, Trauger JW, Spraggon G, Lesley SA et al (2007) Secreted PCSK9 promotes LDL receptor degradation independently of proteolytic activity. *Biochem J* 406: 203–207
22. McNutt MC, Lagace TA, Horton JD (2007) Catalytic activity is not required for secreted PCSK9 to reduce low density lipoprotein receptors in HepG2 cells. *J Biol Chem* 282: 20799–20803
23. Ren G, Rudenko G, Ludtke SJ, Deisenhofer J, Chiu W, Pownall HJ (2010) Model of human low-density lipoprotein and bound receptor based on cryoEM. *Proc Natl Acad Sci USA* 107: 1059–1064
24. Willnow TE, Nykjaer A, Herz J (1999) Lipoprotein receptors: new roles for ancient proteins. *Nat Cell Biol* 1: E157–E162
25. Schneider WJ, Nimpf J (2003) LDL receptor relatives at the crossroad of endocytosis and signaling. *Cell Mol Life Sci* 60: 892–903
26. Brandes C, Novak S, Stockinger W, Herz J, Schneider WJ, Nimpf J (1997) Avian and murine LR8B and human apolipoprotein E receptor 2: differentially spliced products from corresponding genes. *Genomics* 42: 185–191
27. Kim DH, Iijima H, Goto K, Sakai J, Ishii H, Kim HJ, Suzuki H, Kondo H, Saeki S, Yamamoto T (1996) Human apolipoprotein E receptor 2. A novel lipoprotein receptor of the low density lipoprotein receptor family predominantly expressed in brain. *J Biol Chem* 271: 8373–8380
28. Tissir F, Goffinet AM (2003) Reelin and brain development. *Nat Rev Neurosci* 4: 496–505
29. D'Arcangelo G, Miao GG, Chen SC, Soares HD, Morgan JI, Curran T (1995) A protein related to extracellular matrix proteins deleted in the mouse mutant reeler. *Nature* 374: 719–723
30. Yasui N, Nogi T, Kitao T, Nakano Y, Hattori M, Takagi J (2007) Structure of a receptor-binding fragment of reelin and mutational analysis reveal a recognition mechanism similar to endocytic receptors. *Proc Natl Acad Sci USA* 104: 9988–9993
31. Yasui N, Nogi T, Takagi J (2010) Structural basis for specific recognition of reelin by its receptors. *Structure* 18: 320–331
32. Kim DH, Magoori K, Inoue TR, Mao CC, Kim HJ, Suzuki H, Fujita T, Endo Y, Saeki S, Yamamoto TT (1997) Exon/intron organization, chromosome localization, alternative splicing, and transcription units of the human apolipoprotein E receptor 2 gene. *J Biol Chem* 272: 8498–8504
33. Brandes C, Kahr L, Stockinger W, Hiesberger T, Schneider WJ, Nimpf J (2001) Alternative splicing in the ligand binding domain of mouse ApoE receptor-2 produces receptor variants binding reelin but not alpha 2-macroglobulin. *J Biol Chem* 276: 22160–22169
34. Hibi T, Mizutani M, Baba A, Hattori M (2009) Splicing variations in the ligand-binding domain of ApoER2 results in functional differences in the binding properties to Reelin. *Neurosci Res* 63: 251–258
35. Saha S, Boyd J, Werner JM, Knott V, Handford PA, Campbell ID, Downing AK (2001) Solution structure of the LDL receptor EGF-AB pair: a paradigm for the assembly of tandem calcium binding EGF domains. *Structure* 9: 451–456
36. Malby S, Pickering R, Saha S, Smallridge R, Linse S, Downing AK (2001) The first epidermal growth factor-like domain of the low-density lipoprotein receptor contains a noncanonical calcium binding site. *Biochemistry* 40: 2555–2563
37. Arias-Moreno X, Velazquez-Campoy A, Rodriguez JC, Pocovi M, Sancho J (2008) Mechanism of low density lipoprotein (LDL) release in the endosome: implications of the stability and Ca²⁺ affinity of the fifth binding module of the LDL receptor. *J Biol Chem* 283: 22670–22679
38. North CL, Blacklow SC (1999) Structural independence of ligand-binding modules five and six of the LDL receptor. *Biochemistry* 38: 3926–3935
39. Hopkins PN, Wu LL, Stephenson SH, Xin Y, Katsumata H, Nobe Y, Nakajima T, Hirayama T, Emi M, Williams RR (1999) A novel LDLR mutation, H190Y, in a Utah kindred with familial hypercholesterolemia. *J Hum Genet* 44: 364–367
40. Beglova N, Jeon H, Fisher C, Blacklow SC (2004) Cooperation between fixed and low pH-inducible interfaces controls lipoprotein release by the LDL receptor. *Mol Cell* 16: 281–292
41. Yasui N, Kitago Y, Beppu A, Kohno T, Morishita S, Gomi H, Nagae M, Hattori M, Takagi J (2011) Functional importance of covalent homodimer of reelin protein linked via its central region. *J Biol Chem* 286: 35247–35256
42. Leahy DJ, Dann CE III, Longo P, Perman B, Ramyar KX (2000) A mammalian expression vector for expression and purification of secreted proteins for structural studies. *Protein Expr Purif* 20: 500–506
43. Reeves PJ, Callewaert N, Contreras R, Khorana HG (2002) Structure and function in rhodopsin: high-level expression of rhodopsin with restricted and homogeneous N-glycosylation by a tetracycline-inducible N-acetylglucosaminyltransferase I-negative HEK293S stable mammalian cell line. *Proc Natl Acad Sci USA* 99: 13419–13424
44. Fujii Y, Kaneko M, Neyazaki M, Nogi T, Kato Y, Takagi J (2014) PA tag: a versatile protein tagging system using a super high affinity antibody against a dodecapeptide derived from human podoplanin. *Protein Expr Purif* 95: 240–247
45. Stanley P (1989) Chinese hamster ovary cell mutants with multiple glycosylation defects for production of glycoproteins with minimal carbohydrate heterogeneity. *Mol Cell Biol* 9: 377–383
46. Gill SC, von Hippel PH (1989) Calculation of protein extinction coefficients from amino acid sequence data. *Anal Biochem* 182: 319–326
47. Fisher C, Abdul-Aziz D, Blacklow SC (2004) A two-module region of the low-density lipoprotein receptor sufficient for formation of complexes with apolipoprotein E ligands. *Biochemistry* 43: 1037–1044
48. Kabsch W (2010) Xds. *Acta Crystallogr D Biol Crystallogr* 66: 125–132
49. Evans PR, Murshudov GN (2013) How good are my data and what is the resolution? *Acta Crystallogr D Biol Crystallogr* 69: 1204–1214
50. French S, Wilson K (1978) On the treatment of negative intensity observations. *Acta Crystallogr A* 34: 517–525
51. Winn MD, Ballard CC, Cowtan KD, Dodson EJ, Emsley P, Evans PR, Keegan RM, Krissinel EB, Leslie AG, McCoy A et al (2011) Overview of the CCP4 suite and current developments. *Acta Crystallogr D Biol Crystallogr* 67: 235–242
52. Collaborative Computational Project, Number 4 (1994) The CCP4 suite: programs for protein crystallography. *Acta Crystallogr D Biol Crystallogr* 50, 760–763

53. Vagin A, Teplyakov A (1997) MOLREP: an automated program for molecular replacement. *J Appl Cryst* 30: 1022–1025
54. Emsley P, Lohkamp B, Scott WG, Cowtan K (2010) Features and development of Coot. *Acta Crystallogr D Biol Crystallogr* 66: 486–501
55. Murshudov GN, Vagin AA, Dodson EJ (1997) Refinement of macromolecular structures by the maximum-likelihood method. *Acta Crystallogr D Biol Crystallogr* 53: 240–255
56. Chen VB, Arendall WB 3rd, Headd JJ, Keedy DA, Immormino RM, Kapral GJ, Murray LW, Richardson JS, Richardson DC (2010) MolProbity: all-atom structure validation for macromolecular crystallography. *Acta Crystallogr D Biol Crystallogr* 66: 12–21
57. Pape T, Schneider TR (2004) HKL2MAP: a graphical user interface for phasing with SHELX programs. *J Appl Cryst* 37: 843–844
58. Schneider TR, Sheldrick GM (2002) Substructure solution with SHELXD. *Acta Crystallogr D Biol Crystallogr* 58: 1772–1779
59. Bricogne G, Vonrhein C, Flensburg C, Schiltz M, Paciorek W (2003) Generation, representation and flow of phase information in structure determination: recent developments in and around SHARP 2.0. *Acta Crystallogr D Biol Crystallogr* 59: 2023–2030
60. Vonrhein C, Blanc E, Roversi P, Bricogne G (2007) Automated structure solution with autoSHARP. *Methods Mol Biol* 364: 215–230
61. Cowtan KD (2003) The Clipper C++ libraries for X-ray crystallography. *IUCr Comput Comm News* 2: 4–9
62. Nicholls RA, Long F, Murshudov GN (2012) Low-resolution refinement tools in REFMAC5. *Acta Crystallogr D Biol Crystallogr* 68: 404–417
63. Nicholls RA, Fischer M, McNicholas S, Murshudov GN (2014) Conformation-independent structural comparison of macromolecules with ProSMART. *Acta Crystallogr D Biol Crystallogr* 70: 2487–2499
64. Adams PD, Afonine PV, Bunkóczi G, Chen VB, Davis IW, Echols N, Headd JJ, Hung LW, Kapral GJ, Grosse-Kunstleve RW et al (2010) PHENIX: a comprehensive Python-based system for macromolecular structure solution. *Acta Crystallogr D Biol Crystallogr* 66: 213–221
65. Gasteiger E, Hoogland C, Gattiker A, Duvaud S, Wilkins MR, Appel RD, Bairoch A (2005) *The proteomics protocols handbook*. New York: Humana Press: 571–607



License: This is an open access article under the terms of the Creative Commons Attribution-NonCommercial-NoDerivs 4.0 License, which permits use and distribution in any medium, provided the original work is properly cited, the use is non-commercial and no modifications or adaptations are made.